Journal of the Korean Physical Society (2021) 78:1208–1214
https://doi.org/10.1007/s40042-021-00196-x

Online ISSN 1976-8524
Print ISSN 0374-4884

ORIGINAL PAPER

Electronic states of graphene quantum dots induced by nanobubbles

Hee Chul Park[1] · **Minsol Son**[2] · **Seung Joo Lee**[3] · **Nojoon Myoung**[2]

Received: 23 April 2021 / Accepted: 3 May 2021 / Published online: 19 May 2021

Abstract

We analyze the effects of the strain-induced pseudo-magnetic fields (PMFs) originating from nanobubbles (NBs) to examine the possibility for a graphene quantum dot (QD) created by strain engineering. We study the electronic structures and quantum transport properties of graphene subjected to an NB, and report that the presence of PMFs facilitates a strong confinement of Dirac fermions. A circular geometry of the NB locally establishes the characteristic PMFs with C_3 symmetry, resulting in threefold localized states according to the given symmetry. We demonstrate the formation of a graphene QD induced by the NB via the conductance resonances calculated through the NB between opposite quantum Hall edge channels. Analyzing the scattering wavefunctions for the resonances, we confirm the existence of ground and excited states in the graphene QD. In addition, we show a possible valley-polarization in the graphene QD, as a consequence of quantum interference between symmetric and anti-symmetric valley-coupled modes.

Keywords Graphene · Nanobubble · Strain · Quantum dot

1 Introduction

Graphene has been considered as a promising material for next-generation nanoelectronic devices, gifted with outstanding physical properties like a large carrier mobility [1–7], a long mean free path [8–11], and a tunable carrier density via field effects [12, 13]. However, the well-known Klein tunneling that stems from the lack of backscattering in graphene [14–18] limits the control of Dirac fermions with the conventional technologies typically found in metal–oxide–semiconductor field-effect-transistors. Since the gapless nature of graphene disallows the perfect confinement of charge carriers by electrostatic potentials, realizing a quantum dot (QD) in graphene has been a long-awaited achievement over the past decades. Alternative ways of making graphene-based QDs have thus been explored by exploiting the finite band gap in graphene nanoribbons [19–22], bilayer graphene [23–26], or etched graphene nanoconstrictions/nanoflakes [20, 27–29]. In such graphene QD devices, though, the carrier mobility and mean free path are typically reduced compared to monolayer graphene since the pristine properties of graphene are largely affected by edge disorders, interlayer coupling, etc. [30–38].

Otherwise, graphene's outstanding mechanical properties, allowing for elastic deformation up to 20% [39, 40], enable the strain engineering of graphene for potential quantum devices. Since the first experimental evidence for emergent pseudo-magnetic field (PMF)-induced Landau levels [41–43], both measurements and calculations on the effects of PMFs in graphene have progressed toward strain-engineered graphene nanoelectronic devices, especially for valleytronics [43–50]. One previous study suggested the possibility for a QD formation at graphene nanobubbles (NBs) by confirming the existence of a valley-polarized confinement of Dirac fermions due to a strain-induced PMF [50]. Such strain-engineered graphene QDs are advantageous for two reasons. First, the use of a local inhomogeneous PMF does not open a band gap, which is thought to be the main origin of deteriorated coherent transport. Second, the quantum states in a strain-induced QD are able to be adiabatically controlled via the strain engineering of graphene NBs. These

---

✉ Seung Joo Lee
leesj@dongguk.edu

✉ Nojoon Myoung
nmyoung@chosun.ac.kr

[1] Center for Theoretical Physics of Complex Systems, Institute for Basic Science, Daejeon 34051, Republic of Korea

[2] Department of Physics Education, Chosun University, Gwangju 61452, Republic of Korea

[3] Quantum-functional Semiconductor Research Center, Dongguk University, Seoul 04620, Republic of Korea

advantages may pave the way for graphene-based quantum technologies with strain engineering.

In this paper, we investigate the electronic states of a graphene QD produced by the strain-induced PMFs of an NB. We perform numerical calculations on the density of states (DOS) of graphene with an NB by observing the strain-dependent localized states. The formation of the NB-induced QD in graphene is double-checked from resonant tunnelings in the quantum Hall conductance spectra via quantum transport computations based on S-matrix formalism. The scattering wavefunctions extracted from the S matrix are analyzed for an intuitive understanding of how the QD states are given.

2 Model

Let us consider a Gaussian-shaped NB formed in a graphene on a substrate. Its out-of-plane deformation reads

$$z(\vec{r}) = h_0 e^{-(\vec{r}-\vec{r}_0)^2/2\sigma^2}, \tag{1}$$

where h_0 is the maximum deformation at the center of the NB, *i.e.*, at $\vec{r} = \vec{r}_0$, and σ, the standard deviation of the Gaussian shape, implies the radial size of the NB [see Fig. 1b]. Such NBs, in fact, routinely emerge in practical graphene devices when an exfoliated graphene sheet is transferred onto a substrate, as consequences of the substance capture [41, 51, 52]. We note that the circular strain can also be manually created by controlling external forces like Coulomb attraction via gate electrodes [53], gas pressure [54], and mechanical stress [55, 56].

It has been previously discovered that a circularly symmetric deformation leads to a characteristic PMF profile with 120° rotational symmetry, or so-called C_3 symmetry [50, 57]:

$$\vec{\mathcal{B}} = \nu \frac{\hbar\beta}{e a_0} \frac{h_0^2}{\sigma^6} r^3 \sin\theta \hat{z}, \tag{2}$$

where $\nu = \pm 1$ represent different valleys, a_0 is the inter-carbon distance, and $\beta = 3.37$ [50, 58]. Alternatively, the corresponding vector potential induced by the Gaussian-shaped NB can also be calculated through elastic theory in the continuum case [50, 59],

$$\vec{\mathcal{A}}(r,\theta) = \nu \frac{\hbar\beta}{2 e a_0} \left(\frac{h_0}{\sigma^2}\right)^2 r^2 e^{-r^2/\sigma^2} \left(\sin 3\theta \hat{r} + \cos 3\theta \hat{\theta}\right). \tag{3}$$

The profiles of both PMF and its vector potential are shown in Fig. 1c and d.

In this paper, the electronic and transport properties of graphene with an NB are numerically calculated using the tight-binding approach. The Hamiltonian of our system reads

$$H = \sum_{\langle i,j \rangle} t_{ij} a_i^\dagger b_j + \sum_i u_i \left(a_i^\dagger a_i + b_i^\dagger b_i\right) + \text{ h.c. }, \tag{4}$$

where u_i indicates the on-site potential that each sublattice is equally subjected to, and the hopping energy between adjacent sites t_{ij} reads

$$t_{ij} = t\, e^{i\frac{e}{\hbar}\int_i^j \vec{A}\cdot d\vec{r}}\, e^{-\beta\left(\frac{d_{ij}}{a_0}-1\right)}, \tag{5}$$

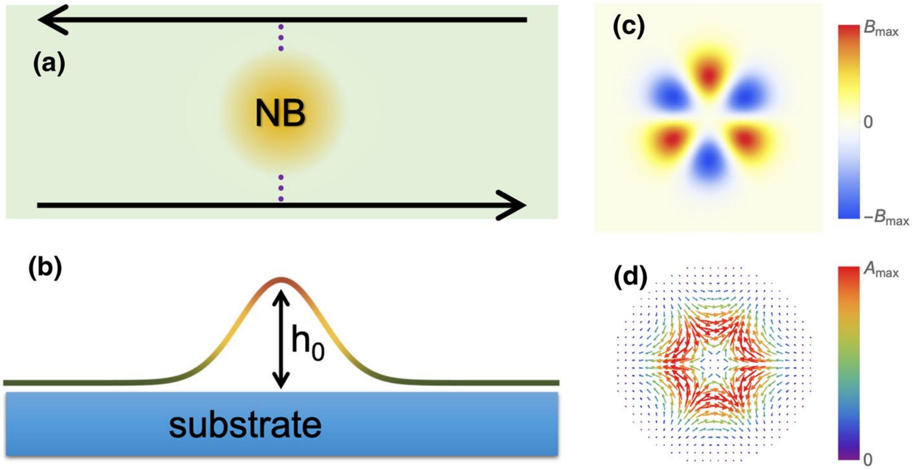

Fig. 1 **a** Schematic of the system. A nanobubble (NB) is located in the center of quantum Hall graphene. Resonant tunneling can occur between the two opposite edge channels via localized states of the strain-induced QD. **b** Side view of the NB in graphene on a substrate. The NB in this study is modelled as Gaussian and characterized by the maximum height h_0. **c** and **d** Profile of a pseudo-magnetic field (PMF) and its corresponding vector potential due to the NB in graphene, being normalized by their maximum values. Note that both oppositely act on Dirac fermions near different valleys

which is determined not only by external magnetic field $\vec{B} = \vec{\nabla} \times \vec{A}$ but also by NB-induced strain with the deformed distance between adjacent carbon atoms d_{ij} normalized by the nearest neighbor distance a_0. In this study, we set the homogeneous magnetic field $\vec{B} = B\hat{z}$ in Landau gauge. The advantage the use of an external magnetic field provides is twofold: i) the states of the NB-induced QD can be clearly distinguished in the quantum Hall insulating phase, and ii) the QD states cnn be efficiently measured by the resonant tunneling between two quantum Hall edge channels along the opposite system boundaries, little perturbing the pristine QD states. In other words, thanks to the presence of the external magnetic field, our system is much simplified compared to the situation where a QD is weakly connected to two identical one-dimensional channels. In our system, Dirac fermions from one channel transfer to the other channel as a result of resonant tunneling through the QD states, as displayed in Fig. 1a.

To explore the electronic states of the NB-induced QD, we perform numerical calculations on the DOS with the S-matrix approach based on the tight-binding model Hamiltonian, using KWANT codes [60]. In addition to the DOS spectra, we examine the properties of the QD states by visualizing the scattering wavefunctions and Dirac fermion flows from the S-matrix of the system. Further, the formation of the strain-induced QD in graphene is confirmed by investigating resonant tunneling in the Landauer–Bütikker conductance achieved from the S-matrix.

3 Results and discussion

3.1 Electronic states of the NB-induced QD

To recognize the emergent localized states by the strain effects, we conducted numerical calculations on the DOS of graphene by varying h_0 for given σ values. Figure 2 displays the resulting DOS spectra. In the absence of the NB, i.e., $h_0 = 0$, it is obvious that the DOS spectra exhibit the typical features of Landau level formation due to the external magnetic field, as shown in Fig. 2. On the other hand, one can also see in the figure that there emerge peaks between the zeroth and first Landau levels in the DOS spectra for finite h_0 values, of which locations tend toward zero energy. The emergent DOS peaks for the finite h_0 values directly indicate that localized states of Dirac fermions can be allowed for the bulk of the quantum Hall insulator.

From Fig. 2, one can additionally recognize that the NB-induced QD hosts not only ground states but also higher order localized states, at sufficiently large h_0. In this context, we also expect that an NB with smaller σ may allow a larger number of localized states since the magnitude of the PMF is determined by the ratio of h_0 and σ. Indeed, for the same value of $h_0 = 20\,a$, the DOS spectrum with $\sigma = 30\,a$ exhibits different numbers of peaks from the case of $\sigma = 20\,a$ (compare the bottom and top panels of Fig. 2).

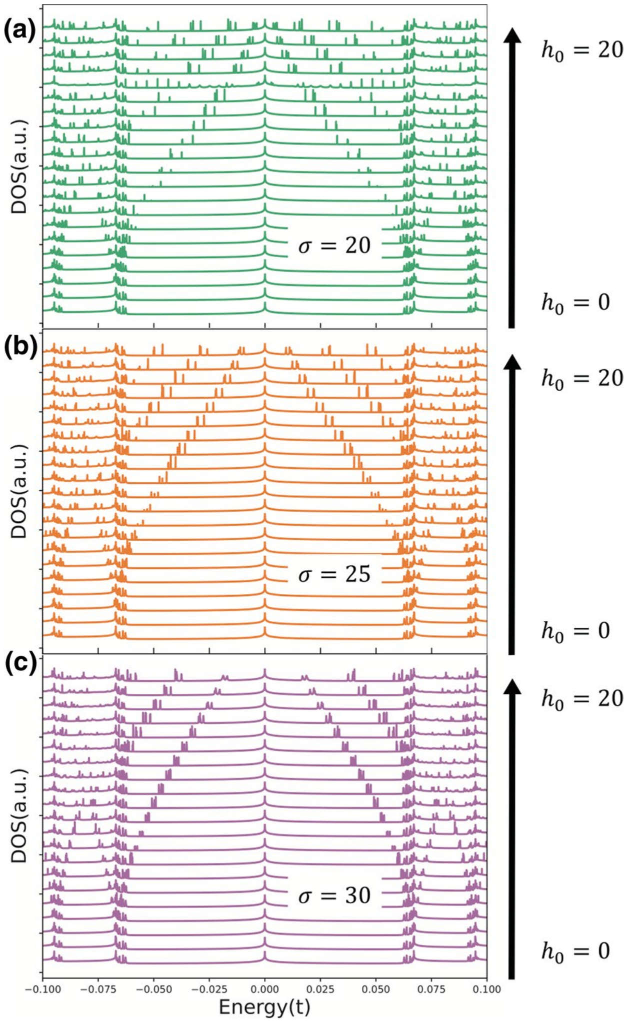

Fig. 2 Densities of states of graphene with a nanobubble as functions of energy by varying the maximum height of the nanobubble h_0 from 0 to 20, for **a** $\sigma = 20$, **b** $\sigma = 25$, and **c** $\sigma = 30$, respectively. Note that h_0 and σ are in units of the lattice constant of graphene $a = \sqrt{3}a_0 = 2.4$ nm, and energy is in units of the hopping term $t = 3$ eV

On the other hand, one can clearly see that there seem to be multiple, rather than singular, NB-induced DOS peaks. Indeed, zooming in on the peaks in the DOS spectra, Fig. 3 shows that the localized states in the NB-induced QD are found to be split into three individual peaks (where each is again split into two peaks, due to the valley degree of freedom mediated by edge–dot coupling [61]). This finding implies that the localized states are threefold by the $\mathcal{C}_3$ symmetry of the PMF profile. The Hamiltonian of our system is expressed as a function of θ:

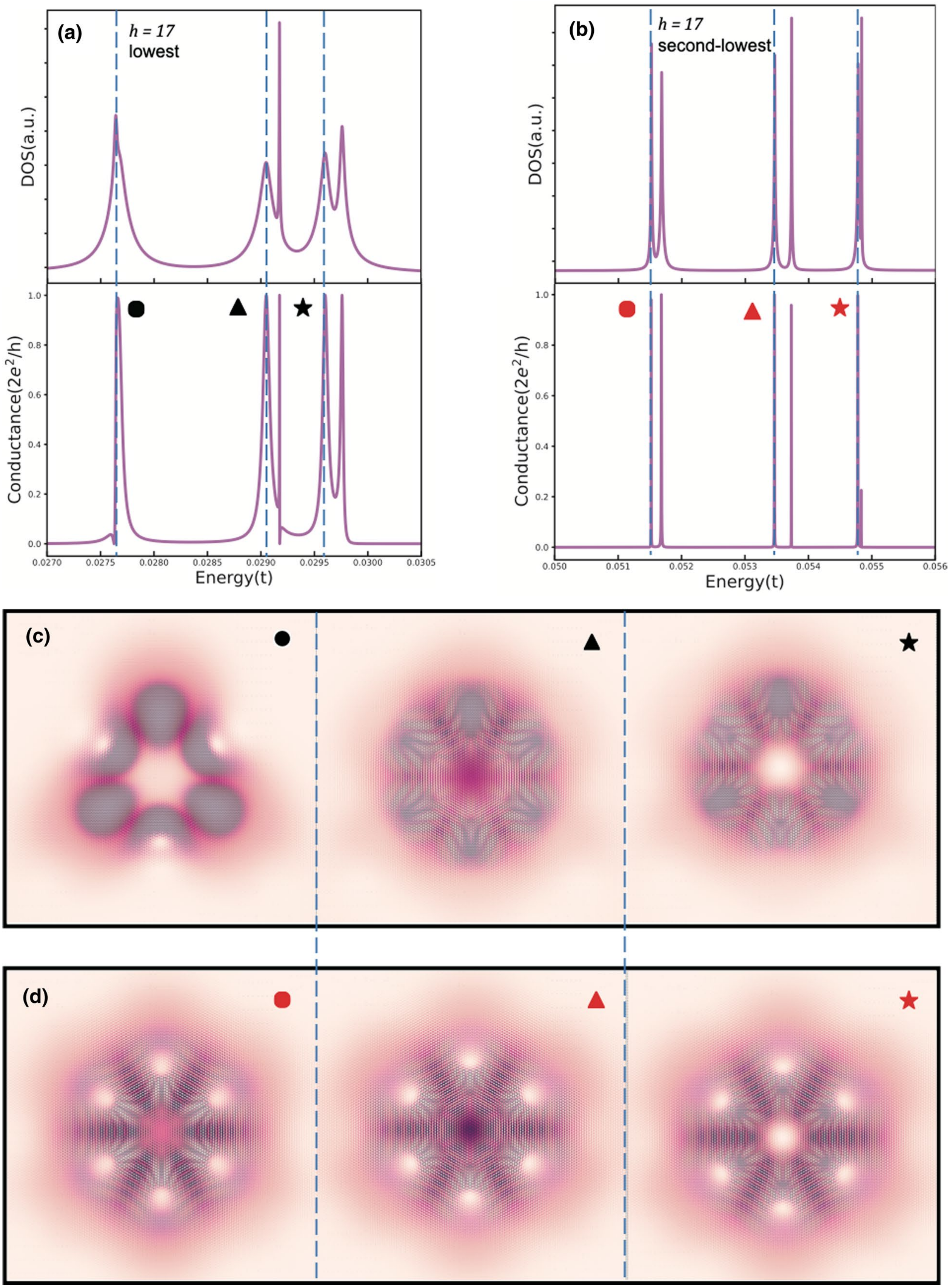
(a)
h = 17
lowest
DOS(a.u.)
Conductance(2e²/h)
1.0
0.8
0.6
0.4
0.2
0.0
0.0270
0.0275
0.0280
0.0285
0.0290
0.0295
0.0300
0.0305
Energy(t)
(b)
h = 17
second-lowest
DOS(a.u.)
Conductance(2e²/h)
1.0
0.8
0.6
0.4
0.2
0.0
0.050
0.051
0.052
0.053
0.054
0.055
0.056
Energy(t)
(c)
(d)

◂**Fig. 3** Comparison of DOS and quantum Hall conductance through **a** the lowest and **b** the second lowest localized states, for $h = 17$. The vertical dashed lines are indicators for the resonant energies. Probability density of the scattering wavefunction at specific resonant energies, for **c** the lowest and **d** the second lowest localized states. The resonant energies are labeled with different markers shown in the conductance spectra. Note that h_0 and σ are in units of the lattice constant of graphene $a = \sqrt{3}a_0 = 2.4$ nm, and energy is in units of the hopping term $t = 3$ eV

$$H(\theta) = v_F\vec{\sigma} \cdot \left[\vec{p} + e\vec{A} + e\vec{\mathcal{A}}(\theta)\right], \tag{6}$$

where the magnetic vector potential $\vec{A}$ due to the external magnetic field can be independent of θ with the choice of an appropriate gauge. Thus, it is clear that the Hamiltonian of the system is accordingly symmetric with respect to 120° rotation. Solutions of the Hamiltonian must satisfy $\mathcal{C}_3$ symmetry and give the quantum number $m = 0$ or ± 1 with respect to θ—a general form of the wavefunctions reads $\Psi(r, \theta) = R(r) \exp(3im\theta)$.

3.2 Resonant tunneling through the NB-induced QD

The formation of the QD as a result of localized Dirac fermions by the PMF can be confirmed by transport measurements from an experimental point of view. Here, we propose a device design to probe the NB-induced QD, exploiting the resonant tunneling between two opposite quantum Hall edge channels. For the quantum Hall effects, conduction in the perpendicular direction to the current injection is able to occur by means of 'hopping' via a number of localized states in the middle of the given device. Likewise, if the NB-induced QD here is located between opposite edge channels in quantum Hall graphene, Dirac fermions can be transferred from one edge to the other through the localized states. In other words, the existence of NBs can mediate charge conduction for quantum Hall conductance measurements. A schematic design of the transport measurement proposal is displayed in Fig. 1a.

For transport calculations, we consider an armchair graphene nanoribbon with a ribbon width of $W = 198\ a$. The effective radius of the strain-induced QD is here set to be $2\sqrt{2}\sigma \simeq 85\ a$ for $\sigma = 30\ a$, i.e., the effective edge–QD distance is about $28\ a$. Since the cyclotron radius is about $13\ a$ under the external magnetic field $B = 32.6$ T, such edge–QD distance is appropriate to produce weak coupling between the edge and the NB-induced QD.

We calculate the conductance between the two edge channels using the S-matrix method and compare the results with the DOS spectra. For comparison, we choose two individual cases: sets of lowest and second lowest energy localized states for $h_0 = 17\ a$, as presented in Fig. 3a and b, respectively. As expected, the conductance spectra evidently exhibit tunneling resonances of which resonant energies are exactly same as those of the DOS peaks. Thus, it is worth remarking that an experimental demonstration of the NB-induced QD is indeed feasible by means of resonant tunneling measurements in the quantum Hall regime. Let us also notice that a splitting of each conductance resonance occurs due to the two-level splitting by the superposition of two valley states [61].

Further, we are able to elucidate the electronic states of the NB-induced QD, theoretically. Wavefunctions of the scattering region can be obtained from the S matrix used for the conductance calculations. Density plots of the scattering wavefunctions are shown in Fig. 3c and d. Among the three localized states, the middle ones correspond to the $m = 0$ case, since the wavefunctions maximize at the center. The spatial distributions of the scattering wavefunctions also satisfy the $\mathcal{C}_3$ symmetry of the system, as expected. Contrary to the lowest energy localized states, the wavefunction distributions for the second lowest energy states are found to have a node in the radial direction, i.e., the second lowest energy states are the excited states in the NB-induced QD, whereas the lowest energy states are the ground states.

Lastly, let us briefly discuss the peculiar appearance of the scattering wavefunction for the lowest energy localized states. In Fig. 3c, the wavefunction distribution for the leftmost resonant peak looks distinct from the others, showing three spots of high probability density, while the others contain six spots.

As aforementioned, the localized states in the NB-induced QD can be valley resolved via interplay between the external magnetic field and the PMF, with the valley-resolved states spatially separating by as much as a 60° rotation [50]. In addition, valley-mixing due to the edge–QD coupling brings about a two-level splitting as a result of the symmetric and anti-symmetric coupling of two valley-resolved localized states [61]. In other words, each of the slightly split peaks depicted in Fig. 3 represents modes with the symmetric or anti-symmetric coupling of two valley-resolved localized states. Then, due to a broadening of the conductance resonances, two scattering wavefunctions corresponding to symmetric/anti-symmetric modes can be substantially overlapped at the resonances. Therefore, in the case of the leftmost localized states in Fig. 3a, a superposition of the symmetric and anti-symmetric modes leads to vanishing wavefunction amplitudes for one valley, while the other valley remains via constructive interference. Consequently, we have valley-polarized QD states, as depicted in Fig. 3c.

Indeed, as shown in Fig. 4, the superposition of the symmetric and anti-symmetric modes gets revoked as the overlap between the conductance resonances disappears. Here, let us notice that the edge–QD distance is defined as $d = W/2 - 2\sqrt{2}\sigma$. As the edge–QD distance increases, the

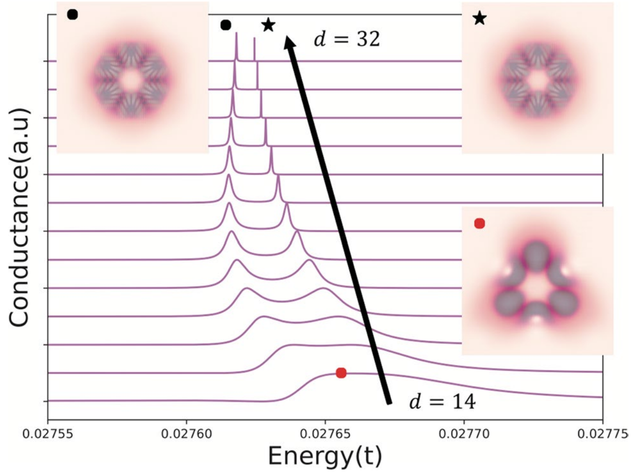

Fig. 4 Conductance spectra for the leftmost resonant tunneling presented in Fig. 3 for various edge–QD distances. The insets represent the probability densities of each resonant state, which are denoted by corresponding markers. Note that, for the lowest spectra, only a single peak is found, i.e., two peaks are exactly converged into one energy. Once again, h_0 and σ are in units of the lattice constant of graphene $a = \sqrt{3}a_0 = 2.4$ nm, and energy is in units of the hopping term $t = 3$ eV

NB-induced QD becomes less perturbed by the edge channel, so the conductance resonances get sharper. Similarly, one can quickly see that the scattering wavefunctions for the second-lowest energy localized states are valley-degenerate like the others, because the second-order resonant peaks are much sharper than those for the ground states.

4 Summary

In this paper, we have theoretically investigated the electronic and transport properties of a nanobubble-induced quantum dot in graphene. If an NB is created in a graphene sample, peaks emerge in the DOS spectra, and the peak positions are shifted by varying the size of the NB (maximum height and radial size). Such findings indicate that the NB can host a number of localized states of Dirac fermions, as if a QD is formed in graphene. Calculating the quantum Hall conductance across the NB in graphene, we have reported clear signatures of NB-induced QD states with the conductance resonances at exactly the same energy as the emergent DOS peaks. Further, analyzing the scattering wavefunctions from the S-matrix, we have examined the properties of the NB-induced QD states. Interestingly, for a given scale of the NB, an accidental valley-polarization occurs as a consequence of the destructive and constructive interference due to the superposition of the symmetric and anti-symmetric valley-coupled modes in the NB-induced QD.

Acknowledgements This work is supported by the National Research Foundation of Korea (NRF-2019R1F1A1051215; NRF2016-R1D1A1B04-935798), Project Code (IBS-R024-D1), and Chosun University (2020). The authors thank Mr. Rasmussen for careful editing of English of the paper.

References

1. A.K. Geim, K.S. Novoselov, Nat. Mater. **6**, 183–191 (2007)
2. D.B. Farmer et al., Nano Lett. **9**, 4474–4478 (2009)
3. C.R. Dean et al., Nat. Nanotechnol. **5**, 722–726 (2010)
4. W. Gannet et al., App. Phys. Lett. **98**, 242105 (2011)
5. P.J. Zomer, S.P. Dash, N. Tombros, B.J. van Wees, App. Phys. Lett. **99**, 232104 (2011)
6. W. Fu et al., Nanoscale **5**, 12104–12110 (2013)
7. L. Banszerus et al., Sci. Adv. **1**, e1500222 (2015)
8. D. Gunlyke, H.M. Lawler, C.T. White, Phys. Rev. B **75**, 085418 (2007)
9. W.-K. Tse, E.H. Hwang, S.D. Sarma, Appl. Phys. Lett. **93**, 023128 (2008)
10. S. Masubuchi et al., Phys. Rev. Lett. **109**, 036601 (2012)
11. A.K. Singh, G. Auton, E. Hill, A. Song, Carbon **84**, 124–129 (2015)
12. Y. Zhang, Y.-W. Tan, H.L. Stormer, P. Kim, Nature (London) **438**, 201–204 (2005)
13. J.R. Williams, L. DiCarlo, C.M. Marcus, Science **317**, 638–641 (2007)
14. M.I. Katsnelson, K.S. Novoselov, A.K. Geim, Nat. Phys. **2**, 620–625 (2006)
15. C.W.J. Beenakker, Rev. Mod. Phys. **80**, 1337 (2008)
16. N. Stander, B. Huard, D. Goldharber-Gordon, Phys. Rev. Lett. **102**, 026807 (2009)
17. J.M. Pereira, F.M. Peeters, A. Chaves, G.A. Farias, Semicon. Sci. Tech. **25**, 033002 (2010)
18. P.E. Allain, J.N. Fuchs, Eur. Phys. J. **83**, 301 (2011)
19. F. Sols, F. Guinea, A.H.C. Neto, Phys. Rev. Lett. **99**, 166803 (2007)
20. K.A. Ritter, J.W. Lyding, Nat. Mater. **8**, 235–242 (2009)
21. C. Stampfer et al., Phys. Rev. Lett. **102**, 056403 (2009)
22. S. Wang et al., Nano Lett. **17**, 4277–4283 (2017)
23. J.M. Pereira, P. Vasilopoulos, F.M. Peeters, Nano Lett. **7**, 946–949 (2007)
24. J. Velasco Jr. et al., Nano Lett. **18**, 5104–5110 (2018)
25. A. Kurzmann et al., Phys. Rev. Lett. **123**, 026803 (2019)
26. L. Benazerus et al., Nano Lett. **20**, 7709–7715 (2020)
27. K. Todd, H.-T. Chou, S. Amasha, D. Goldharber-Gordon, Nano Lett. **9**, 416–421 (2009)
28. C. Volk et al., Nat. Commun. **4**, 1753 (2013)
29. R. Yan et al., RSC Avd. **4**, 13097–23106 (2014)
30. J.B. Oostinga et al., Phys. Rev. B **81**, 193408 (2010)
31. M.-W. Lin et al., Phys. Rev. B **84**, 125411 (2011)
32. A. Yazdanpanah et al., IEEE Trans. Electron Dev. **59**, 433–440 (2012)
33. J. Baringhaus et al., Appl. Phys. Lett. **106**, 043109 (2015)
34. J. Aprojanz et al., Nat. Commun. **9**, 4426 (2018)
35. J.B. Oostinga et al., Nat. Mater. **7**, 151–157 (2008)
36. S.D. Sarma, E.H. Hwang, E. Rossi, Phys. Rev. B **81**, 161407(R) (2010)
37. H. Zhou et al., Nat. Commun. **4**, 2096 (2013)
38. S. Engels et al., Phys. Rev. Lett. **113**, 126801 (2014)
39. C. Lee, X. Wei, J.W. Kysar, J. Hone, Science **321**, 385–388 (2008)
40. E. Cadelano et al., Phys. Rev. Lett. **102**, 235502 (2009)
41. N. Levy et al., Science **329**, 544–547 (2010)

42. E.V. Castro, M.A. Cazalilla, M.A.H. Vozmediano, Phys. Rev. B **96**, 241405(R) (2015)
43. S.-Y. Li, Y. Su, Y.-N. Ren, L. He, Phys. Rev. Lett. **124**, 106802 (2020)
44. T. Low, F. Guinea, Nano Lett. **10**, 3551–3554 (2010)
45. Z. Wu et al., Phys. Rev. Lett. **106**, 176802 (2011)
46. Y. Jiang et al., Phys. Rev. Lett. **110**, 046601 (2013)
47. J. Wang, K.S. Chan, Z. Lin, Appl. Phys. Lett. **104**, 013105 (2014)
48. V. Torres, P. Silva, E.A.T. de Souza, L.A. Silva, D.A. Bahamon, Phys. Rev. B **100**, 205411 (2019)
49. C.-C. Hsu, M.L. Teague, J.-Q. Wang, N.-C. Yeh, Sci. Adv. **6**, eaat9488 (2020)
50. N. Myoung, H. Choi, H.C. Park, Carbon **157**, 578–582 (2020)
51. J. Lu, A.H.C. Neto, K.P. Loh, Nat. Commun. **3**, 823 (2012)
52. H. Ghorbanfekr-Kalashami, K.S. Vasu, R.R. Nair, F.M. Peeters, M. Neek-Amal, Nat. Commun. **8**, 15844 (2017)
53. H. Ochoa, E.V. Castro, M.I. Katsnelson, F. Guinea, Phys. E **44**, 963–966 (2012)
54. A.D. Smith et al., ACS Nano **10**, 9879–9886 (2016)
55. R. Roldán, A. Cstallanos-Gonez, E. Cappeluti, F. Guinea, J. Phys. Condens. Matter **27**, 313201 (2015)
56. D.G. Papageorgiou et al., Nanoscale **12**, 2228–2267 (2020)
57. N.N. Klimov et al., Science **336**, 1557–1561 (2012)
58. M.R. Masir, D. Moldovan, F.M. Peeters, Solid State Commun. **175–176**, 76–82 (2013)
59. R. Carillo-Bastos, M. Ochoa, S.A. Zavala, F. Mireles, Phys. Rev. B **98**, 165436 (2018)
60. C.W. Groth, M. Wimmer, A.R. Akhmerov, X. Waintal, New. J. Phys. **16**, 063065 (2014)
61. N. Myoung, J.-W. Ryu, H.C. Park, S.J. Lee, S. Woo, Phys. Rev. B **100**, 045427 (2019)

Publisher's Note Springer Nature remains neutral with regard to jurisdictional claims in published maps and institutional affiliations.